

A New Photobioreactor for Continuous Microalgal Production in Hatcheries Based on External-Loop Airlift and Swirling Flow

Karine Loubière,¹ Erell Olivo,² Gael Bougaran,² Jérémy Pruvost,¹ René Robert,³ Jack Legrand¹

¹Laboratoire GEPEA UMR CNRS 6144, CRTT, Boulevard de l'Université, BP 406, 44602 Saint-Nazaire Cedex, France; telephone: 33-2-40-17-26-68; fax: 33-2-40-17-26-18; e-mail: jeremy.pruvost@univ-nantes.fr

²Laboratoire Physiologie et Biotechnologie des Algues, IFREMER Centre de Nantes, Nantes Cedex, France

³Laboratoire de Physiologie des Invertébrés, IFREMER, Station Expérimentale d'Argenton, Presqu'île du Vivier, Argenton en Landunvez, France

Received 11 February 2008; revision received 13 May 2008; accepted 13 June 2008

Published online 18 July 2008 in Wiley InterScience (www.interscience.wiley.com). DOI 10.1002/bit.22035

ABSTRACT: This study deals with the scale of a new photobioreactor for continuous microalgal production in hatcheries. The combination of the state-of-art with the constraints inherent to hatcheries has turned the design into a closed, artificially illuminated and external-loop airlift configuration based on a succession of elementary modules, each one being composed of two transparent vertical interconnected columns. The liquid circulation is ensured pneumatically (air injections) with respect to a swirling motion (tangential inlets). A single module of the whole photobioreactor was built-up to scale its geometry (diameter and length) and to optimize its design (air sparger, tangential inlets). The volumetric productivities were predicted by modeling radiative transfer and growth of *Isochrysis affinis galbana* (clone Tahiti). The hydrodynamics of the liquid phase was modeled in terms of global flow behavior (circulation and mixing times, Péclet number) and of swirling motion decay along the column (Particle Image Velocimetry). The aeration performances were determined by overall volumetric mass transfer measurements. Continuous cultures of *Isochrysis affinis galbana* (clone Tahiti) were run in two geometrical configurations, generating either an axial or a swirling flow. Lastly, the definitive options of design are presented as well as a 120-L prototype, currently implemented in a French mollusk hatchery and commercialized.

Biotechnol. Bioeng. 2009;102: 132–147.

© 2008 Wiley Periodicals, Inc.

KEYWORDS: continuous photobioreactor; hatchery; airlift; swirling flow; *Isochrysis affinis galbana*

Introduction

With regard to their taxonomic diversity and plasticity, photosynthetic microorganisms are a natural resource with high potential, thus attracting scientific and industrial attention. Their development can be separated into either, direct use of biomass or indirect use for the production of high-value compounds and for environmental applications (wastewater treatment, hydrogen or biodiesel production) (Richmond, 2004; Spolaore et al., 2006). Their production under controlled conditions implies a specific reactor, named photobioreactor, which mainly differs from classical bioreactors by the need of a light supply, these microorganisms being photoautotrophic. Light cannot be considered as a common substrate insofar as it involves two antagonist phenomena: on the one hand, a high amount of photonic energy is required to ensure microalga growth conditions, but on the other hand, the increase of the biomass concentration in the reactor decreases the light penetration depth in the culture due to cell self-shading. Thus, the use of light in the culture is the major constraint in photobioreactors, which makes their scale-up difficult and often limits the production of concentrated biomass with high quality and productivity. The literature describes a great diversity of photobioreactors, often classified into plane and cylindrical/tubular geometrical configurations (Carvalho et al., 2006), showing that no a priori ideal geometry exists.

In the present study, the application targeted is aquaculture and more particularly mollusk hatcheries. Microalgae are here used to feed broodstock, larvae and spat, and have then to be regularly produced in large amounts

Correspondence to: J. Pruvost

(Coulteau and Sorgeloos, 1992). According to a survey that we have conducted in the main six hatcheries of the French West Coast, microalgal production represented in 2002, for flagellate microalgae, from 400 to 6,000 billion cells per day, and for diatoms, from 900 to 20,000 billion cells per day. The microalgae commonly cultivated for mollusks are *Isochrysis affinis galbana*, *Pavlova lutheri*, *Chaetoceros muelleri*, *Chaetoceros calcitrans*, *Thalassiosira pseudonana*, *Skeletonema marinoi* (Borowitzka, 1997). For Pacific cupped oyster *Crassostrea gigas* larvae, a bi-specific diet is rather privileged for the youngest larvae: *Isochrysis affinis galbana* is then associated with a complementary microalga which is different from one hatchery to another (Rico-Villa et al., 2006). At present, microalgal production in French hatcheries is mainly performed by means of batch culture systems consisting of vertical aerated column PMMA reactors. Their major drawbacks are a partial control of biomass quality and quantity, low productivities, contamination, manpower intensive (frequent handling and cleaning operations), biofouling.

To improve this situation, the present work proposes a new photobioreactor for continuous microalgal production in hatcheries. The constraints to integrate for the design are: to ensure a continuous production adjustable to hatchery requirements, to be a closed and artificially illuminated system, to have a design as simple as possible for minimizing fabrication cost, price and floor-space, to be robust (marine atmosphere) and easy to clean. From that, a preliminary choice of geometrical configuration has been realized: it consists of a succession of elementary modules, each one being composed of two transparent vertical interconnected columns. The liquid phase circulation is performed pneumatically, namely by gas injections placed at the column bottom and uniformly dispatched in the whole photobioreactor. Thus, each elementary module can be seen as an external loop airlift photobioreactor, except that the outlet of the downcomer is connected to the next module. In addition, as already used in annular (Muller-Feuga et al., 2003a,b; Pruvost et al., 2002) and torus photobioreactors (Pottier et al., 2005), a swirling motion will be generated (tangential inlets) in order to minimize the biofilm formation at walls. The major interest of this design is not only to enable closed, artificially illuminated and continuous microalgal culture to be easily performed, but also modularity in volume to be satisfied without scaling-up/down calculations. Indeed, the illumination device will be designed so as to conserve the same illuminated specific surface (ratio of the illuminated surface to the culture volume) whatever the numbers of modules, implying that, for a given incident flux and a fixed dilution rate, the volumetric productivity will remain identical for a single module and for a multimodule photobioreactor. As a consequence, the number of elementary modules will only be conditioned by the microalgal production required. This is an essential advantage with regard to the variability of hatchery sizes and phytoplankton productions.

This study reports results of various investigations carried out to scale the geometry of this photobioreactor (column diameter and length) and to optimize its design (air sparger, tangential inlets). A single module of the whole photobioreactor is built up to test the influence of various parameters. The column diameter constitutes a key parameter as controlling the light distribution inside the culture: it will be chosen in accordance with the predictions of volumetric productivities (coupled modeling of radiative transfer and photosynthetic growth). The column height is mainly dependent on the decay of swirling motion along the column and on its efficiency to limit biofouling at walls; that is why the effects of air flow rate, air sparger and tangential inlets on hydrodynamics will be investigated (tracing, PIV). Moreover, the aeration performances will be determined by overall volumetric mass transfer measurements. Lastly, continuous cultures of the microalga *Isochrysis affinis galbana* (clone Tahiti) will be run in two geometrical configurations, generating either an axial or a swirling motion; they will enable the volumetric productivities and the biofouling deposited to be compared. In conclusion, the definitive options of design will be expressed and a 120-L prototype presented.

Materials and Methods

Description of the Experimental Set-Up

The single-module photobioreactor consists of an external-loop airlift made of transparent PMMA to allow effective light penetration and a clear visual observation (Fig. 1a). This device is composed of two vertical columns connected by two flanges, the column above the air sparger being called the riser and the other one the downcomer. Liquid circulation is induced by the hydrostatic unbalance caused by the density difference between the gassed and ungassed liquid columns. These columns are of equal sizes with a 0.03 m radius R , a 1 m liquid height H_L . The total liquid volume V_L is 6.1 L. Note that the downcomer column is machined in a cubic transparent block to minimize optical distortion for PIV measurements.

The swirling motion is induced by tangential inlets inside each column (Legentilhomme and Legrand, 1991). For that, specific connection flanges are designed by means of prism-shaped inserts of different sizes introduced in the body of the flange (Fig. 1b). The three geometrical configurations of flanges investigated are characterized by Velocity Factors VF equal to 1, 4 and 9, where $VF1$ generates an axial motion inside columns (no prism insert). This latter parameter, VF , is defined as the ratio of the injection velocity at the flange outlet to the mean velocity at the flange inlet (Legentilhomme and Legrand, 1991), namely between the sections at the flange inlet and outlet (Fig. 1c).

Two air spargers are tested (Fig. 1a): a capillary (2 mm in diameter) located tangentially to the wall of the riser base (noticed T), and an elastic multi-perforated membrane

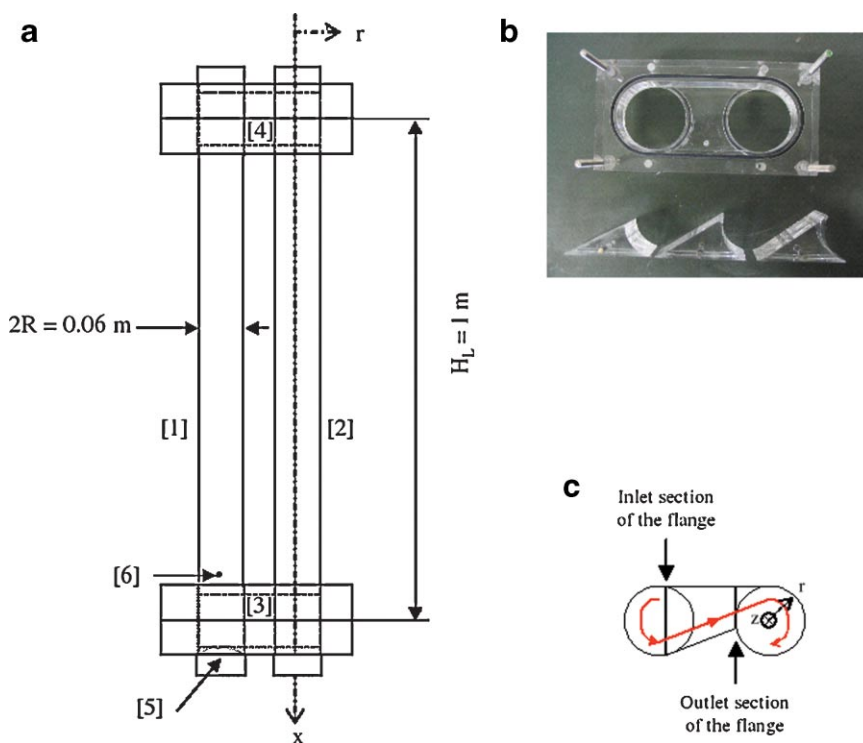


Figure 1. a: Schematic representation of the single-module photobioreactor: [1] riser column, [2] downcomer column, [3] lower connection flange, [4] upper connection flange, [5] membrane sparger, [6] capillary sparger. b: Photograph showing the body of a connection flange and the prism-shaped inserts defining the Velocity Factors VF_2 , VF_4 , and VF_9 (left–right). c: Schematic representation of a connection flange (swirling motion generation). [Color figure can be seen in the online version of this article, available at www.interscience.wiley.com.]

recovering the entire column section (denoted M). The air flow rates Q_G vary between 0.1 and 1.6 NL min⁻¹. The superficial velocities U_G are then very low, ranging from 2.2 to 9.4 mm s⁻¹. The associated specific power input in the reactor P_G/V_L (Chisti, 1989) varies from 11 to 43 W m⁻³. Note that no bubbles are observed in the downcomer and that the average gas hold-up is always below 1% (qualitative measurements).

Hydrodynamics of the Liquid Phase

Tracer Measurements

A pulse of tracer (seawater) is injected in front of the inlet of the lower connection flange, and is detected by a platinum conductimetric probe located inside this flange, flushed with wall. The variation in conductance, directly proportional to tracer concentration, is measured by a conductimeter Tacussel[®] CD810 coupled with a data acquisition device and a computer. These tracer experiments are performed in water, for three Velocity Factors (VF_1 , VF_4 , VF_9), for both air spargers and for seven air flow rates.

Particle Image Velocimetry

This technique is applied to characterize the swirling motion and its decay along the downcomer height where no bubble

entrainment occurs. A Dantec[®] device is used with a laser Nd-YAG New Wave Solo (15 mJ/pulse). The light pulses are synchronized with a CCD camera (Dantec Dynamics Flow Sense M2/E 8 bits, 1600 × 1186 pixels²) equipped with an objective Nikon 60 mm. These images are analyzed with the Flow Manager[®] software to obtain velocity fields. The tracer is made of polyamide particles (Dantec Invent[®] 38A2121) with a mean diameter of 50 μm (concentration close to 0.1 g L⁻¹). The image calibration is ensured by using sighting marks placed inside the downcomer whose dimensions are known. To determine the swirl intensity, instantaneous velocity fields are measured, inside the downcomer, in rx -planes (Fig. 2) at different radial positions (r equal to -0.025, -0.02, -0.01, 0, 0.01, 0.02, and 0.025 m) and axial positions (x equal to 0.05, 0.15, 0.25, 0.4, 0.55 and 0.85 m). For a given operating condition, an average of 200 image acquisitions is required to calculate time-averaged velocity fields. The image post-treatment is equivalent to the one performed by Pruvost et al. (2000). Finally, the radial profiles of axial and tangential components of time-averaged velocity (noted $U(r)$ and $W(r)$ respectively) are obtained at different heights, x , in the downcomer. It is important to precise that, according to the measurement planes, the tangential component of velocity, W , can be only known in the vertical symmetrical plane of the downcomer (Pruvost et al., 2000). In Figure 2a, the locations where they are calculated are represented by black

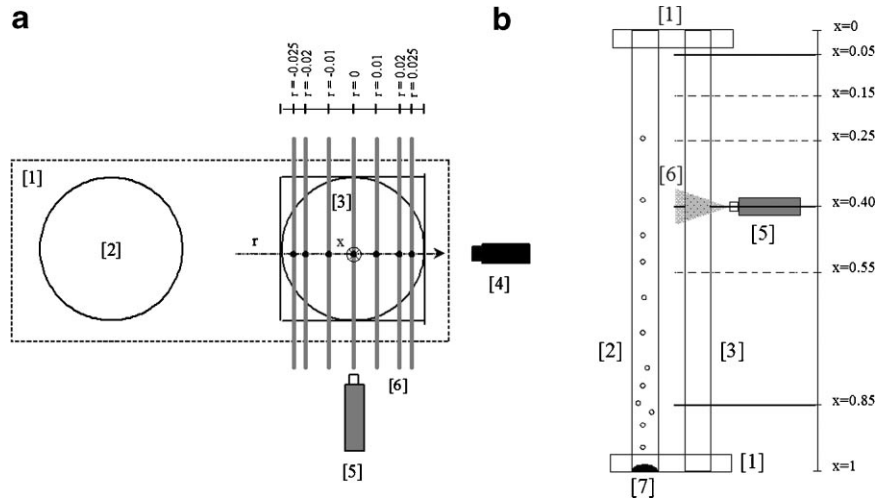


Figure 2. Top view (a) and Front view (b) of the PIV set-up: [1] flanges, [2] riser column, [3] downcomer column, [4] CCD Camera, [5] laser beam generator, [6] laser sheet, [7] air sparger.

points. In practice, for one given axial position x , the radial profiles of tangential components, $W(r)$, are reconstructed from data measured in the rx -planes acquired at different radial positions r (Fig. 2a). These PIV experiments are carried out in seawater, for two Velocity Factors ($VF4$, $VF9$), both air spargers and two air flow rates ($Q_G = 0.74$ and 1.6 NL min^{-1}).

Gas–Liquid Mass Transfer

The well-known dynamic gassing-in and gassing-out method is used to measure overall volumetric gas–liquid mass transfer coefficients $k_L a$ (Roustan, 2003). After removing oxygen from the liquid phase (nitrogen bubbling), air flow is established and the time-variation of C_L followed, until saturation, by means of an oxygen probe (Mettler Toledo[®] O_2 InPro 6800) placed at the top of the downcomer column and connected to a transmitter (Mettler Toledo[®] O_2 InPro 4100). During this reoxygenation step, the mass balance in dissolved oxygen concentration is:

$$\frac{dC_L}{dt} = k_L a (C_L^* - C_L) \quad (1)$$

where C_L^* is the dissolved oxygen concentration at saturation (at 25°C and at the oxygen partial pressure in air under atmospheric pressure, it is equal to 8.3 mg L^{-1} for tap water and to 6.9 mg L^{-1} for seawater and Conway medium). The dynamics of the oxygen probe can be described using a first-order differential equation (Ingham et al., 1994) as:

$$\frac{dC_p}{dt} = \frac{1}{t_p} (C_L - C_p) \quad (2)$$

where C_p is the dissolved oxygen concentration inside the probe. The time constant of the oxygen probe, t_p , is measured using a method based on probe response to negative oxygen steps (Vandu et al., 2004), and found equal to 14 s. This latter value is negligible when compared to mass transfer characteristic times, $1/k_L a$, the minimum of which is here 73 s.

Finally, the overall volumetric mass transfer coefficient is accurately determined by solving the following equation resulting from the combination of Equation (1) with Equation (2):

$$\frac{C_p}{C_L^*} = 1 + \left(\frac{\exp(-k_L a \cdot t) - k_L a \cdot t_p \cdot \exp(-t/t_p)}{k_L a \cdot t_p - 1} \right) \quad (3)$$

The mass transfer experiments are run for three liquid phases (tap water, seawater, Conway medium), three Velocity Factors ($VF1$, $VF4$, $VF9$), both air spargers and five air flow rates. For all these conditions, the usual assumptions associated with Equation (1) (i.e., a perfectly mixed liquid phase, a constant gas composition between the reactor inlet and outlet) are verified.

Algal Cultures

Microalga and Culture Medium

Because it is used in French mollusk hatcheries, *Isochrysis affinis galbana* (clone Tahiti) is selected for this study. Under the reference CCAP 927/14, it was obtained from the phytoplanktonic collection of Oban (Scotland). The algal nutritive medium consists of natural seawater (originated from the coastal area of Saint-Malo in France, aged in the dark during 1 month, filter-sterilized through a $0.22 \mu\text{m}$

Table I. Composition of the Conway medium.

Principal elements	(FeCl ₃ , 6H ₂ O): 1.3 g; (MnCl ₂ , 4H ₂ O): 0.36 g; (H ₃ BO ₃): 33.6 g; (Na ₂ -EDTA, 2H ₂ O): 49.8 g; (NaH ₂ PO ₄ , 2H ₂ O): 26 g; (NaNO ₃): 100 g
Metal	(ZnCl ₂): 0.021 g; (CoCl ₂ , 6H ₂ O): 0.02 g; ((NH ₄) ₆ Mo ₇ O ₄ ² , 4H ₂ O): 0.009 g; (CuSO ₄ , 5H ₂ O): 0.02 g
Vitamins	B1 (thiamine aneurine hydrochloride): 0.2 g; B12 (cyanocobalamine): 0.01 g

The mass reported (in g) is defined per Liter of distilled water, the medium being prepared with 1 mL of each solution per Liter of seawater.

pore-size filter) enriched in Conway medium at 1 mL/L of seawater (Table I).

Growth Curve

The growth curve of the microalga *Isochrysis affinis galbana*, $\mu(G)$, has to be determined for predicting productivity. For that, the planar torus photobioreactor described by Pottier et al. (2005) and Pruvost et al. (2006) is used. The cultures are run in turbidostat mode. A low cellular concentration (10^9 cell L⁻¹) is maintained to minimize the effects of mutual shading. Indeed, to display accurate results, it is important to differentiate the incident light, q_O , measured behind the reactor surface from the averaged irradiance, G , really received by the culture. Knowing cell concentration inside the reactor, G is calculated by integrating, along the culture depth z , the attenuation profile of irradiance predicted by the radiative transfer model (see Theoretical Developments below). As a very low concentration is maintained in the torus reactor, the incident and averaged lights are very close, and thus the potential error induced by the model becomes negligible. Note that such method remains valid only if the incident light flux is kept in an acceptable range. Indeed, due to low cell densities, high incident light flux would induce photoinhibition effects not encountered in standard production conditions where higher biomass concentration and thus attenuation phenomena are achieved.

This torus photobioreactor is illuminated by a set of 10 daylight fluorescent tubes (OSRAM L13W/12-950, diameter 16 mm), fixed on a framework to keep them parallel. For a given distance between light source and torus reactor, the incident light flux q_O is measured, without microalgal culture, behind the front surface of the reactor, by means of a spherical quantum sensor (LICOR US-SQS/A Heinz Walz). Four measurement points are considered to calculate an average value of q_O . Once the culture has reached equilibrium, the averaged growth rate $\langle\mu\rangle$ is determined, and according to previous comments, can be associated to the real irradiance G received by microalgae. The *Isochrysis affinis galbana* growth curve is here established for q_O ranging from 15 to 400 $\mu\text{mol m}^{-2} \text{s}^{-1}$.

Continuous Cultures

The single-module photobioreactor is sterilized by a peroxyacetic acid solution (5%, 20 min). The microalgal

inoculum leads to an initial concentration close to 10^9 cell L⁻¹. Continuous cultures are run in chemostat mode: a KNF Stepdos[®] pump is used for medium renewal while the culture is harvested by overflowing. *Isochrysis affinis galbana* cultures are run in two geometrical configurations to compare biological performances using an axial or a swirling motion. Thus, two identical pilots are used simultaneously: the first is equipped with VF1-shaped flanges and the second with VF4-shaped flanges. Apart from VF, the other conditions are similar. The dilution rate D is set to 0.36 day^{-1} , but daily controlled. The temperature is regulated at $27 \pm 1^\circ\text{C}$ (thermoregulated room), and the pH maintained at 7.2 ± 0.1 by automatic injection of CO₂ (solenoid valve). The average incident light flux q_O on the reactor surface is equal to $250 \pm 10 \mu\text{mol m}^{-2} \text{s}^{-1}$. The air sparger is the capillary located tangentially to the wall of the riser base, and the air flow rate is fixed at 1.4 NL min^{-1} . Cell concentration, X , is daily measured by cellular counting (Malassez cell), as well as the nitrate and phosphate residual concentrations (ionic chromatography) to verify that no substrate limitation occurs. For each VF condition, the continuous cultures are run three times. Lastly, the volumetric productivity P_X is calculated by the product between X and D at equilibrium. To compare both configurations, the biofouling at walls is also visually observed.

Radiative-Field Measurements

The single-module photobioreactor is illuminated by 10 fluorescent tubes (Grolux[®] F58W/GRO-T8, OSRAM Sylvania Co., Munich, Germany), horizontally disposed and spaced 12 cm from each other. For different distances between reactor and tubes, the incident light flux q_O behind the curved surface of the reactor is measured as a function of the angular position θ_C (from $-\pi/2$ to $\pi/2$). These measurements are performed, without culture, by using a spherical quantum sensor (LICOR US-SQS/A Heinz Walz, 3 mm in diameter), and will serve as initial conditions in the light transfer modeling (see Theoretical Developments Section). Moreover, the attenuation profile of irradiance is experimentally determined for $X = 1.7 \times 10^{10}$ cell L⁻¹ and for $q_O = 210 \mu\text{mol m}^{-2} \text{s}^{-1}$. For these experiments, the underwater spherical quantum sensor is displaced radially inside the column (with an increment equal to 4.5 mm), and a black shield is placed around the column half circumference opposite the light source to avoid wall reflections.

Theoretical Developments

Productivity Prediction and Radiative Transfer Modeling

In steady state regime, the volumetric microalgal productivity, P_X , is expressed as:

$$P_X = \langle \mu \rangle X = DX \quad (4)$$

where $\langle \mu \rangle$ is the average growth rate. For photosynthetic growth, μ depends on the irradiance received G . Both absorption and scattering phenomena led to heterogeneous radiative field inside the culture. Therefore, the determination of $\langle \mu \rangle$ imposes to calculate first the attenuation profile along the culture depth, $G(z)$. The coupling with *Isochrysis affinis galbana* growth curve then enables the local growth kinetics $\mu(G(z))$ and so $\langle \mu \rangle$ to be deduced.

As in Cornet et al. (1995), a two-flux formulation of the general theory of radiative transfer is used to determine the irradiance field. Based on an one-dimensional light attenuation hypothesis and assuming both a quasi-collimated field of radiation and a normal incidence, the irradiance profile along a direction z is then calculated by the following analytical expression (Pottier et al., 2005; Pruvost et al., 2008):

$$G(z) = 2q_0(\theta_C) \frac{(1 + \alpha) \cdot \exp(\delta(L - z)) - (1 - \alpha) \cdot \exp(-\delta(L - z))}{(1 + \alpha)^2 \cdot \exp(\delta L) - (1 - \alpha)^2 \cdot \exp(-\delta L)} \quad (5)$$

where,

$$\alpha = \sqrt{\frac{E_a}{(E_a + 2bE_s)}}, \quad \delta = (E_a + 2bE_s)\alpha X \quad (6)$$

In contrast to the planar torus photobioreactor of Pottier et al. (2005), the present airlift geometry has a cylindrical-shaped surface. In this case, due to refraction effects induced by curvature, the direction of the light attenuation flux is no more unique: when passing across the curvature, light rays are deviated from their initial direction. This phenomenon has been integrated into the light transfer modeling of Pottier et al. (2005), by considering: (i) the distribution of incident light flux at the curvature boundaries, $q_0(\theta_C)$ (see Materials and Methods Section), (ii) the Snell-Descartes law to calculate, for each incident light ray impinging the reactor optical surface, its new direction z inside the culture and the associated light path length L . The refraction phenomenon leads to intersections inside the culture between several light directions: in this case, the resulting irradiance is calculated as the sum of irradiances obtained at the intersection point.

The accurate formulation of this radiative transfer model needs to determine the optical properties of the culture. Pottier et al. (2005) computed the optical properties of the

microalga *Chlamydomonas reinhardtii*, by means of a powerful predictive method based on the Lorenz-Mie theory and on a preliminary knowledge of microalga pigment contents, size and shape. The same approach is applied here for *Isochrysis affinis galbana* by considering a mean diameter of 5 μm , a mean cellular mass of 7.64 pg and an ovoid shape (image analysis). Issued from literature data (Green and Leadbeater, 1994), the pigment composition (weighted percent) is: chlorophyll-a 2%, chlorophyll-b 0%, chlorophyll-c 0.6%, photoprotective carotenoids (fucoxanthine, diadinoxanthine, diatoxanthine, caroten) 2.4%. Finally, the optical properties of *Isochrysis affinis galbana* are the following:

$$E_a = 293 \text{ m}^2 \text{ kg}^{-1} \quad E_s = 757 \text{ m}^2 \text{ kg}^{-1} \quad b = 0.01162 \quad (7)$$

Global Flow Modeling

From tracer measurements, the hydrodynamic behavior is modeled by an axial dispersed plug flow with total recirculation, thereby enabling the mean circulation time t_C and the axial dispersion coefficient D_{ax} to be determined. This model, commonly used in the case of swirling flows (Benkhelifa et al., 2000), is expressed by:

$$\frac{C(\theta)}{C_\infty} = \frac{1}{2} \sqrt{\frac{Pe_L}{\pi\theta}} \sum_{j=-\infty}^{+\infty} \exp\left(-\frac{Pe_L(j + z^* - \theta)^2}{4\theta}\right) \quad (8)$$

The mean circulation time, t_C , is optimized, as well as the Péclet number Pe_L and the geometrical factor z^* , by fitting Equation (8) with the experimental curve using the Nelder-Mead algorithm. The optimization is considered valid if the mean standard deviation (between calculated and experimental responses) is between 0.05 and 0.1. The mean circulation velocity, U_C , is then calculated by:

$$U_C = \frac{L_t}{t_C} \quad (9)$$

The mixing time t_m is defined with respect to a homogeneity degree equal to 95%.

Characterization of Swirling Decaying Flows

Even if swirling decaying flows are extremely complex (three-dimensional, non-axi-symmetrical and non-established with regard to the axial position), the swirl intensity can be quantified according to the swirl number Sn . This dimensionless parameter represents the axial flux of swirl momentum divided by the product between the axial flux of axial momentum and the column diameter (Gupta et al.,

1984), and is given by:

$$Sn = \frac{\int_{-R}^R UW_r^2 dr}{2R \int_{-R}^R U^2 r dr} \quad (10)$$

It is particularly useful to study the decay of the swirling motion with the axial position from the swirl inducer, this decay is often correlated by an empirical exponential law as:

$$Sn = a' \exp\left(\frac{-b'}{2R}\right) \quad (11)$$

where a' and b' are empirical coefficients linked to the initial swirling intensity and the motion decay respectively.

Results and Discussion

Theoretical Productivity

Validation of the Radiative Transfer Modeling

For $q_0 = 210 \mu\text{mol m}^{-2} \text{s}^{-1}$ and $X = 1.7 \times 10^{10} \text{ cell L}^{-1}$, Figure 3 reports the predicted attenuation profiles along the culture depth with the measured irradiances. The integration of refraction effects in the modeling is positive: a better agreement between experimental and predicted irradiances occurs when optical distortion is considered. Although the model tends to underestimate the attenuation at the back optical side, these results are widely acceptable, especially with regard to the geometrical complexity (curved surface)

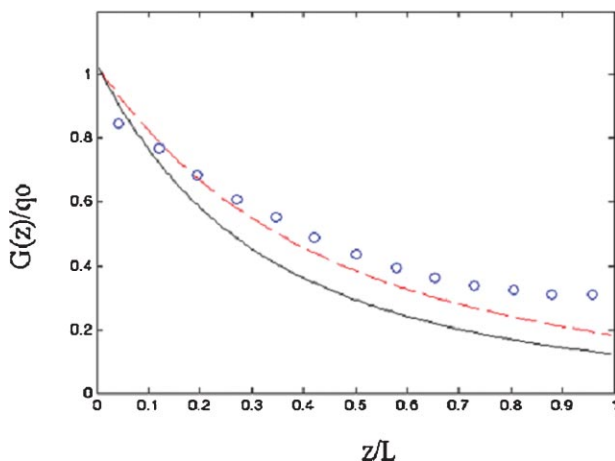


Figure 3. Attenuation profiles of irradiances $G(z)/q_0$ along the culture depth z/L ($L = 60 \text{ mm}$), for $q_0 = 210 \mu\text{mol m}^{-2} \text{s}^{-1}$ and $X = 1.7 \times 10^{10} \text{ cell L}^{-1}$, without (solid line) and with (dashed line) taking optical distortion into account, the experimental irradiances being represented by blue circle symbols (\circ). [Color figure can be seen in the online version of this article, available at www.interscience.wiley.com.]

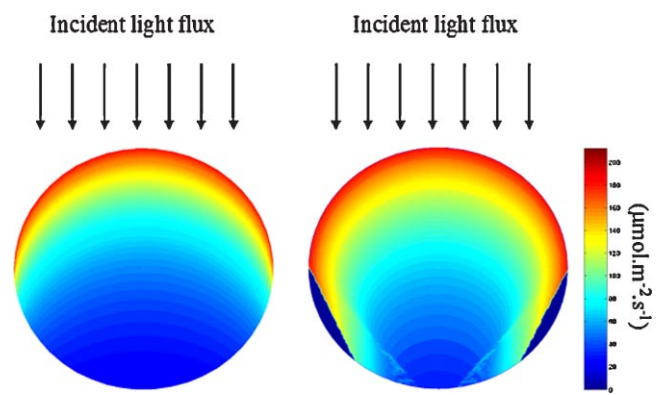


Figure 4. Irradiance fields over the column section for $q_0 = 210 \mu\text{mol m}^{-2} \text{s}^{-1}$ and $X = 1.7 \times 10^{10} \text{ cell L}^{-1}$, without (left side) and with (right side) taking optical distortion into account. [Color figure can be seen in the online version of this article, available at www.interscience.wiley.com.]

and the simplifying assumptions emitted (collimated incident light, approximate optical properties). Figure 4 gives an example of predicted irradiance fields over the column section whether refraction effects are considered or not. Important differences are highlighted: light ray refraction slows down light dilution inside the culture and reduces the proportion of slightly illuminated zones. This is directly linked to the irradiance over-concentrations generated near walls on light source side. Such results are in agreement with the attenuation profiles observed in Figure 3.

Isochrysis Affinis Galbana Growth Curve

The experimental specific growth rates μ of *Isochrysis affinis galbana* are reported in Figure 5 as a function of the irradiance received G . As no photoinhibition is experimen-

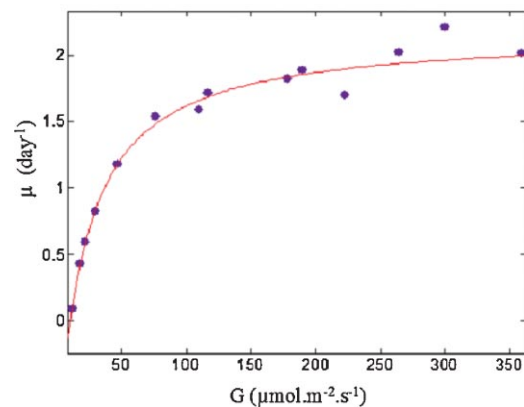


Figure 5. Specific growth rate μ of *Isochrysis affinis galbana* versus irradiance G received (solid line: model; symbol " \bullet ": experimental data). [Color figure can be seen in the online version of this article, available at www.interscience.wiley.com.]

tally observed below $360 \mu\text{mol m}^{-2} \text{s}^{-1}$, a simple model based on a Monod law is chosen to describe the growth curve:

$$\mu = \mu_{\max} \frac{G}{K_G + G} - \mu_m \quad (12)$$

Calculated by a multi-parametric regression based on experimental data, these parameters are: $\mu_{\max} = 3.12 \text{ day}^{-1}$, $\mu_m = 0.93 \text{ day}^{-1}$, $K_G = 25.6 \mu\text{mol m}^{-2} \text{s}^{-1}$. The compensation irradiance G_C (determined from Equation (12) when $\mu = 0$) is then equal to $10.9 \mu\text{mol m}^{-2} \text{s}^{-1}$. The latter value is rather in agreement with literature: Falkowski et al. (1985) found G_C equal to $16 \mu\text{mol m}^{-2} \text{s}^{-1}$, Molina Grima et al. (1997) to $10 \mu\text{mol m}^{-2} \text{s}^{-1}$ and Tzovenis et al. (2003) to $8 \mu\text{mol m}^{-2} \text{s}^{-1}$. Molina Grima et al. (1997) determined a maintenance term μ_m close to the present one, 0.92 day^{-1} versus 0.93 day^{-1} respectively. Nevertheless, an important variability is observed for the inhibiting irradiance: although no photoinhibition appears here, Sukenik and Wahnou (1991) have reported that *Isochrysis affinis galbana* is saturated at $300 \mu\text{mol m}^{-2} \text{s}^{-1}$ and inhibited at $500 \mu\text{mol m}^{-2} \text{s}^{-1}$; according to Molina Grima et al. (1997), the growth optimum varies from 820 to $1620 \mu\text{mol m}^{-2} \text{s}^{-1}$, the photoinhibition occurring over. These results remain difficult to interpret and to compare because: (i) light measurement methods are different and/or not precised, (ii) the time during which microalgae are submitted to a given incident flux is not well defined, (iii) the light flux considered is often the one emitted by light source or measured at the reactor surface and not the irradiance really received by microalgae (dependent of the biomass concentration).

Predicted Productivity

The microalgal productivity is predicted according to Equation (4) where $\langle \mu \rangle$ is the average of the local growth kinetics, $\mu(G(z))$, solved by coupling the two-flux radiative transfer model, Equations (5)–(7), and the *Isochrysis affinis galbana* growth curve, Equation (12). Figure 6a reports, for $q_0 = 250 \mu\text{mol m}^{-2} \text{s}^{-1}$, the predicted productivity, P_X , as a function of dilution rate, D , and of the column radius, R . Whatever the column radius, the variation looks similar and is characterized by an optimum obtained for a dilution rate D close to 0.035 h^{-1} (0.84 day^{-1}). These optimal volumetric productivities result from an equilibrium maximizing both cell concentration and culture harvest flow rate. They are very sensitive to the column radius, a drastic decrease being observed for increasing radii. Figure 6b presents, at the dilution rate chosen for experiments ($D = 0.36 \text{ day}^{-1}$), the variations of the volumetric productivity with the column radius, for three incident light flux. It clearly appears that, especially for low radii, the incident light flux has a major influence: for $R = 0.03 \text{ m}$, P_X is close to $3.0 \times 10^{10} \text{ cell L}^{-1} \text{ day}^{-1}$ for $250 \mu\text{mol m}^{-2} \text{s}^{-1}$, to $2.5 \times$

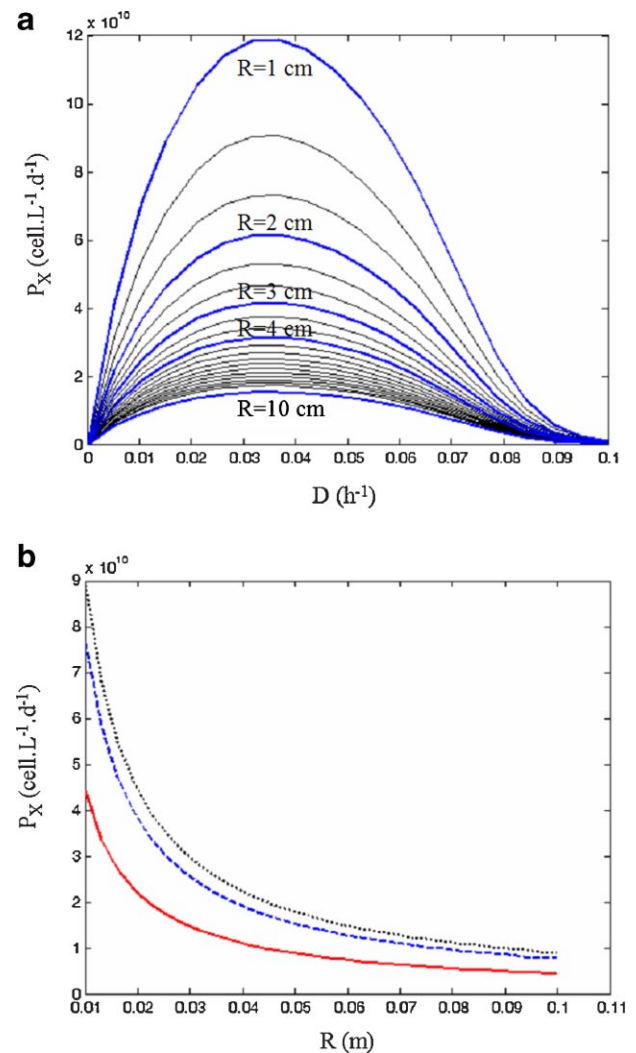


Figure 6. Predicted volumetric productivity: (a) as a function of dilution rate and column radius, for $q_0 = 250 \mu\text{mol m}^{-2} \text{s}^{-1}$, (b) as a function of column radius for dilution rate $D = 0.36 \text{ day}^{-1}$ and for several incident light flux: $q_0 = 100 \mu\text{mol m}^{-2} \text{s}^{-1}$ (solid line), $200 \mu\text{mol m}^{-2} \text{s}^{-1}$ (dashed line) and $250 \mu\text{mol m}^{-2} \text{s}^{-1}$ (dotted line). [Color figure can be seen in the online version of this article, available at www.interscience.wiley.com.]

$10^{10} \text{ cell L}^{-1} \text{ day}^{-1}$ for $200 \mu\text{mol m}^{-2} \text{s}^{-1}$ and to $1.5 \times 10^{10} \text{ cell L}^{-1} \text{ day}^{-1}$ for $100 \mu\text{mol m}^{-2} \text{s}^{-1}$.

For designing the multimodule photobioreactor, these predictions are very useful: knowing the daily larval needs in microalgae, the photobioreactor volume theoretically required can be easily calculated for each column radius and incident light flux. A survey has been conducted in the main six hatcheries of the French West Coast (all being devoted to the Pacific cupped oyster *Crassostrea gigas*). The data collected have shown that the production of *Isochrysis affinis galbana* required is close to $1.2 \times 10^{12} \text{ cell day}^{-1}$ (this is an average value which can significantly vary depending on hatchery sizes). Using these data, the photobioreactor volume theoretically required is ranging from 50 to 130 L (for $2 < R < 5 \text{ cm}$ and $100 < q_0 < 200 \mu\text{mol m}^{-2} \text{s}^{-1}$). It

increases for increasing radii and for decreasing incident flux. Using low column radii offers, on the one hand, the undeniable advantage to reduce the photobioreactor volume (higher productivities), but on the other hand, presents the drawback to multiply the number of columns and connection flanges, which is economically disadvantageous. These results indicate that the optimal column diameter should be mainly chosen from a compromise between productivity and building cost prices, even though other factors, such as floor-space or cleaning simplicity, should also be taken into account. Finally, the complete integration of various parameters converges towards a column radius equal to 0.03 m (study not detailed).

Hydrodynamics of the Liquid Phase

The aim being to design a multimodule photobioreactor for hatcheries, no advanced modeling on hydrodynamics will be proposed here: the investigations will therefore be restricted to the characterization of the global flow behavior and of the swirling motion decay. Note that comparisons with literature on airlift reactors will remain, in general, difficult because the characteristics of the present airlift are original: very low superficial gas velocity (below 1 cm s^{-1}), external-loop with columns of equal sizes, swirling motion.

Global Flow Behavior

In Figure 7a, the mean circulation velocities U_C are plotted as a function of superficial gas velocity U_G , for several Velocity Factors and air spargers. They are significantly larger when the motion inside the reactor is axial rather than swirling, or in other words, when the Velocity Factor decreases. This is directly linked to the increase of pressure drops due to section restrictions inside the connection flanges. When compared to Velocity Factor, the kind of air spargers has a minor influence on the mean circulation velocities: the membrane sparger (M) tends to generate slightly higher velocities than the capillary located tangentially to the column (T), probably resulting from larger gas retentions. As in Chisti (1989), the previous variations of U_C with U_G can be described by an empirical relation based on a power law (see Table II).

The mean circulation times, t_C , are reported in Table II. They clearly highlight how the swirling flow enables the

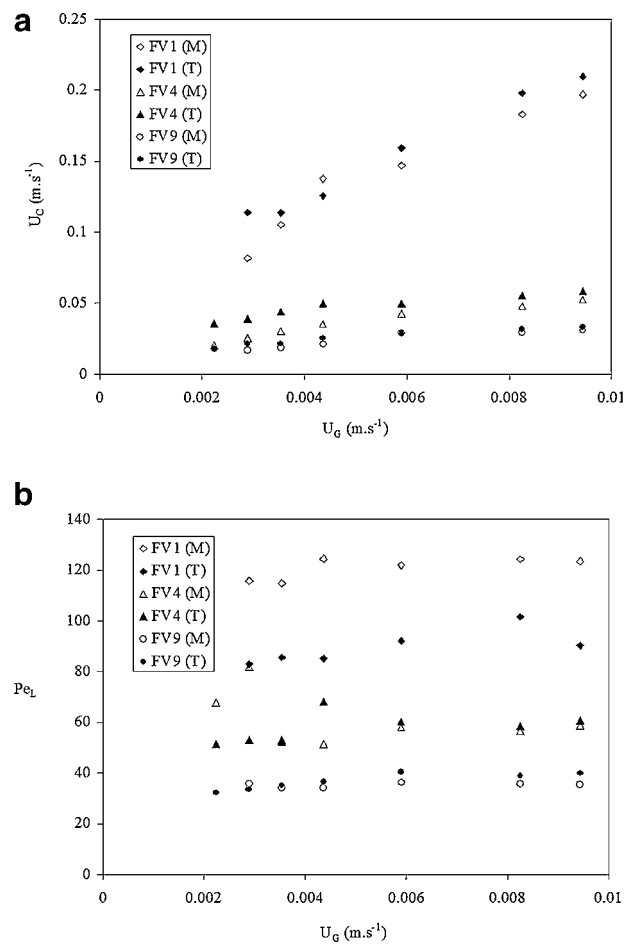


Figure 7. Mean circulation velocity (a) and Péclet number based on the mean reactor length (b) versus superficial gas velocity for several Velocity Factors and air spargers (T : capillary placed tangentially to the column; M : membrane).

time necessary for fluid to cover one reactor loop to be significantly increased, when compared to a purely axial motion. In Table II are also reported the ratios, averaged over the range of air velocity, of mixing time to mean circulation time. They decrease for increasing Velocity Factors: generating a swirling flow, instead of an axial one, then enables the number of loops necessary to reach a perfectly mixed state to be reduced. The mixing ability of the reactor is thus enhanced thanks to swirling motion.

Table II. Data issued from the global flow modeling ($2.2 < U_G < 9.4 \text{ mm s}^{-1}$).

Air sparger	VF (-)	$\frac{U_C = \omega \cdot U_G^v}{\omega}$		t_C (s)	$\langle t_m/t_C \rangle$ (-)	D_{ax} ($\text{m}^2 \text{s}^{-1}$)	Re_L (-)
T	1	3.02	0.57	20.4–11.1	11.7	0.12–0.21	6.8×10^3 – 1.3×10^4
	4	0.27	0.33	64.7–39.6	6.8	0.06–0.09	2.1×10^3 – 3.5×10^3
	9	0.24	0.42	130.7–70.1	4.0	0.05–0.07	1.1×10^3 – 2×10^3
M	1	5.05	0.69	28.4–11.8	—	0.06–0.14	4.9×10^3 – 1.2×10^5
	4	1.08	0.64	113.5–44.1	5.6	0.03–0.08	1.2×10^3 – 3.1×10^3
	9	0.41	0.54	138.5–75.4	3.7	0.04–0.08	10^3 – 2×10^3

Figure 7b presents the Péclet number (defined on the mean reactor length) as a function of the superficial air velocity. Whatever the conditions, no noticeable variation of Péclet number with air velocities is observed. In contrast, the Velocity Factor induces a significant decrease of Pe_L (or a rise of the axial dispersion coefficient D_{ax} , see Table II) with increasing VF . This shows that the motion behavior goes from a plug type flow ($Pe_L > 100$ for $VF1$) to a mixed type flow, thus confirming thus that swirling motion enables the mixing to be improved.

Swirling Flow Characterization

First of all, for each operating condition, it has been verified that, when the radial profiles of axial velocity components are integrated along the column diameter, the mean circulation velocity deduced is conserved whatever the axial positions, and is equal to the one calculated by tracer measurements (Eq. 9). These calculations make the velocity field measurements valid, even if they have been only performed for a single angular position θ_C .

Figure 8a and b plot typical radial profiles of velocity components at different axial positions. These curves illustrate that the main movement responsible for swirling motion is controlled by the tangential component, which decreases with increasing axial positions but always remains greater than the axial component. The latter observation is

particularly important to prove that the designed tangential inlets are efficient to generate a swirling flow along the full column height. As already observed in annular photobioreactors using swirling flows (Pruvost et al., 2000), the extremes of both axial and tangential velocities are located near the walls and tend to shift towards the center of the column for increasing axial positions. This is explained by the centrifugal force effects induced by the tangential inlet that diminish as far as the distance from the connection flange increases. In contrast to annular configurations, negative axial velocities are present in the central area of the column, giving evidence of flow recirculations. They are highly pronounced at the top of the column and disappear more downstream; their existence enables the increase of tangential component generated by the centrifugal force to be counterbalanced (Aoubed et al., 1994). Note that, when air flow rate increases, all these behaviors are conserved or become acute (data not reported). Lastly, the comparison between Figure 8a and b logically shows that smaller axial components and greater tangential components are obtained for $VF9$ than for $VF4$.

The curves of the swirl number Sn as a function of the axial position x are given in Figure 9. As aforementioned (Fig. 8), the attenuation of the swirling motion is here clearly demonstrated whatever the operating conditions. It is essential to note that this decay is significant at the bottom of the column but not complete. Except near the tangential

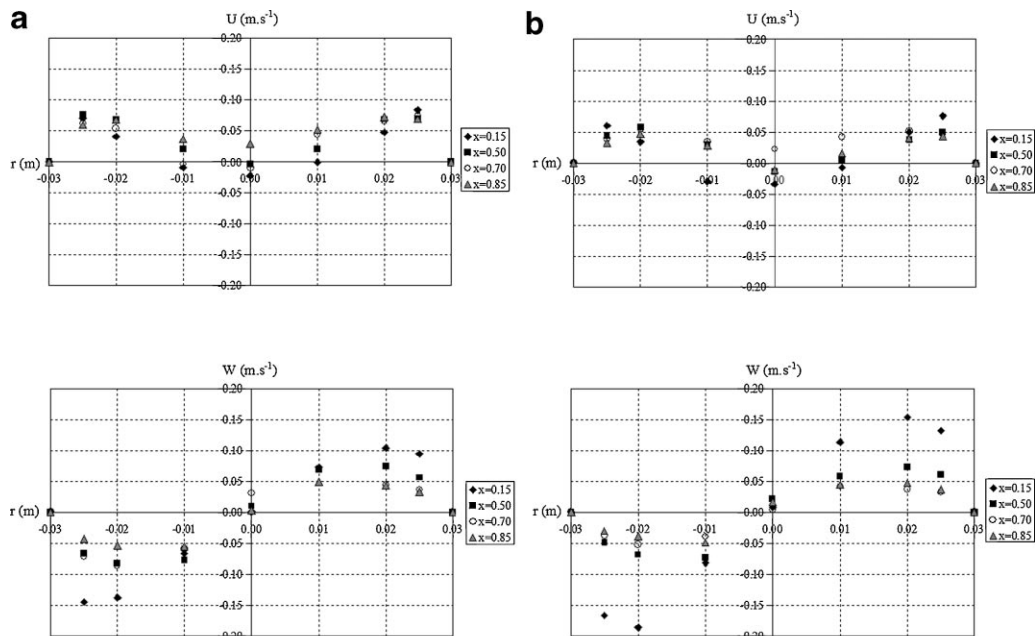


Figure 8. Radial profiles of axial- (top) and tangential- (bottom) components of velocity inside the downcomer column at different axial positions x from the upper connection flange (membrane sparger; $Q_G = 1.6 \text{ NL min}^{-1}$): (a) $VF4$ (b) $VF9$.

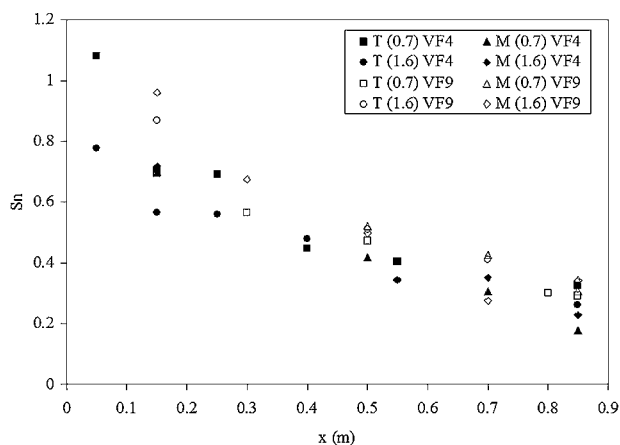


Figure 9. Swirl number as a function of axial position from the tangential inlet. The air flow rates (in NL min^{-1}) is put in brackets, *T* and *M* referring to air sparger type.

inlet, no major difference is found between both Velocity Factors and air flow rates. As a consequence, the decay of the swirling motion is modeled by a unique exponential law with $a' = 0.920$ and $b' = 0.086$ (Eq. 11).

The conclusion to be drawn from these results is that, independently of air sparger and air flow rate, both Velocity Factors, *VF4* and *VF9*, ensure the conservation of swirling motion along the full column height. The attenuation being yet significant, it seems more reasonable to impose, for the multimodule photobioreactor, a column height which does not exceed 1 m.

Gas-Liquid Mass Transfer

The variations of the volumetric gas-liquid mass transfer coefficient with the superficial air velocity are plotted in

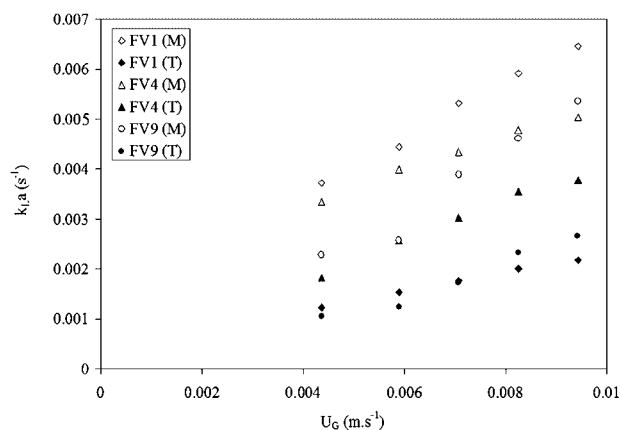


Figure 10. Volumetric gas-liquid mass transfer coefficient as a function of superficial air velocity in the case of tap water.

Figure 10 with tap water as liquid phase. Whatever the operating conditions, $k_L a$ can be correlated with U_G according to a power law (Wu et al., 1992):

$$k_L a = \beta U_G^\delta \quad (13)$$

The values of the empirical coefficients, β and δ , are reported in Table III. Beyond this, it is interesting to note that, whatever the Velocity Factors, the membrane sparger (*M*) induces volumetric mass transfer coefficients two to three times higher than the capillary sparger (*T*). This is directly related to the fact that the membrane sparger generates smaller bubble sizes and higher gas retentions than the capillary one, thus producing higher interfacial areas. The mass transfer performances of such a sparger are widely recognized (Hébrard et al., 1996; Loubière et al., 2003) and are here reinforced by the fact that all the bubbles formed at the exit of the membrane orifices are collected under the influence of the swirling motion inside an air column which, about twenty centimeters above, bursts into a swarm of very small spherical bubbles (below 1 mm). This phenomenon does not exist with the capillary as, contrary to the membrane punctured over its entire surface sheet, this sparger is located tangentially to the wall at the column base and generates only one train of large bubbles (spherical cap shape, above 10 mm) rising along the column wall according to trajectories which follow the main streamlines induced by the swirling motion.

Figure 10 also shows the influence of the Velocity Factor on the volumetric mass transfer coefficients. For the membrane, the swirling motion has a negative impact: when compared to *VF1*, $k_L a$ is reduced by a factor varying between 1.1 and 1.3 for *VF4*, and between 1.6 and 1.2 for *VF9*. In contrast, for the capillary sparger, the greatest coefficients are obtained for *VF4*, whereas *VF1* and *VF9* lead to similar values. These tendencies remain difficult to analyze without quantitative measurements for bubble sizes and gas retentions. Nevertheless, the hypothesis that can be put forward concerns the mechanisms of bubble formation at the sparger which are: (i) fundamentally different depending on the air sparger type (one train of large bubbles against an air column bursting into small bubbles), and (ii) susceptible to be disturbed according to the nature and the intensity of the liquid motion produced at the exit of the connection flange.

For superficial gas velocities varying from 0.004 to 0.010 m s^{-1} , Table III reports the ratio of the volumetric mass transfer coefficients measured, either in the Conway medium (CM) or in seawater (SW), to the ones in tap water (TW). For the capillary sparger (*T*), these ratios are almost constant and close to 1 whatever the Velocity Factors: the physico-chemical properties of sea media do not therefore modify the aeration performances of this sparger, probably due to the large sizes of the bubbles produced. This is not the case with the membrane sparger where $k_L a$ are two to four times higher in presence of seawater and Conway

Table III. Data issued from gas–liquid mass transfer measurements ($4 < U_G < 10 \text{ mm s}^{-1}$).

Air sparger	VF (–)	$k_L a = \beta \cdot U_G^{\delta}$		$(k_L a)_{CM}/(k_L a)_{TW}$	$(k_L a)_{SW}/(k_L a)_{TW}$
		$\beta _{TW}$	$\delta _{TW}$		
T	1	0.071	0.75	1.02–0.98	1.05–1.03
	4	0.35	0.96	0.90–1.07	0.84–1.10
	9	1.00	1.28	0.94–0.76	0.99–0.88
M	1	0.20	0.73	2.23–1.79	2.09–1.76
	4	0.062	0.54	2.82–2.64	3.16–2.60
	9	1.34	1.19	3.85–2.25	2.90–2.56

medium, this phenomenon being more pronounced when VF increases. These tendencies should also here come from the bubble formation mechanisms.

Lastly, whatever the operating conditions, the volumetric gas–liquid mass transfer coefficients vary between 0.001 s^{-1} and 0.013 s^{-1} in Conway medium. For design purposes, it is now interesting to qualitatively compare these aeration performances with the oxygen produced photosynthetically by the microalga *Isochrysis affinis galbana*. The single-module photobioreactor was not equipped to follow either the dissolved oxygen concentration or the gas composition during the microalgal cultures. Consequently, a Chlorolab2[®] system (Hansatech Instruments[®]) has been used to estimate, under controlled conditions of temperature and irradiance, both respiration and photosynthesis (liquid phase measurements). It reveals that the oxygen production by *Isochrysis affinis galbana* is almost $6 \times 10^{-10} \mu\text{mol O}_2 \text{ cell}^{-1} \text{ min}^{-1}$ at an irradiance of $250 \mu\text{mol m}^{-2} \text{ s}^{-1}$. The continuous cultures run in the single-module photobioreactor have lead to a cellular concentration of $4.26 \times 10^{10} \text{ cell L}^{-1}$ at equilibrium for this incident light flux (Fig. 11). Using this value, an oxygen production of $25.5 \mu\text{mol L}^{-1} \text{ min}^{-1}$ is deduced. If, by a very simple approach, this production is directly extrapolated to the

total liquid volume of the single-module photobioreactor ($V_L = 6.1 \text{ L}$), a flow rate of oxygen produced equal to 0.083 mg s^{-1} is obtained. In parallel, the oxygen physically transferable from liquid to gas phases (namely by desorption) is expressed by:

$$N_{O_2} = k_L a \cdot V_L (C_P - C_L^*) \quad (14)$$

where C_L^* is here equal to 6.9 mg L^{-1} (Conway medium, 25°C , P_{atm}). By substituting 0.083 mg s^{-1} into Equation (14) and by considering the worst and the best aeration performances ($k_L a = 0.001$ and 0.013 s^{-1} respectively), the exchange potentials, $\Delta C = C_P - C_L^*$, necessary to remove all the oxygen produced are then ranging from 13 to 1 mg L^{-1} . In view of these low values, it is reasonable to conclude that the single-module photobioreactor will be able to evacuate the oxygen produced. Consequently, for such geometrical configuration of photobioreactor, the microalgal growth will not be a priori limited by gas–liquid mass transfer, whatever the operating conditions that could be retained in the end. Nevertheless, to definitively conclude on this point, more advanced investigations have to be conducted, based, in particular, on oxygen in situ measurements (both liquid and gas phases) during cultures.

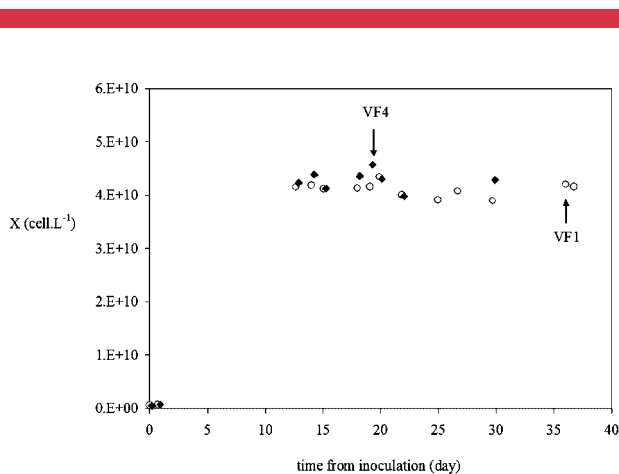


Figure 11. Typical growth curves of *Isochrysis affinis galbana* (cellular concentration versus time from inoculation), in the cases where an axial flow (VF1) and a swirling flow (VF4) are generated inside the single-module photobioreactor ($q_0 = 250 \mu\text{mol m}^{-2} \text{ s}^{-1}$, $D = 0.36 \text{ d}^{-1}$, $Q_G = 1.4 \text{ NL min}^{-1}$, capillary sparger).

Continuous Microalgal Cultures

Isochrysis affinis galbana continuous cultures are compared depending on whether an axial (VF1) or a swirling flow (VF4) is generated inside the single-module photobioreactor, the other experimental conditions being similar (see Materials and Methods Section). Typical growth curves are plotted in Figure 11 for both Velocity Factors. The nature of the flow induced inside the photobioreactor has no effect on the cellular concentration at equilibrium: in both cases, after almost 15 days, the cultures reach an equilibrium corresponding to $4.3 \times 10^{10} \pm 0.2 \times 10^{10} \text{ cell L}^{-1}$ which is maintained until the cultures are stopped on day 40. The experimental volumetric productivities are calculated at the equilibrium: no significant difference is detected between both VF1 and VF4, leading to an average productivity of $1.64 \times 10^{10} \pm 3 \times 10^8 \text{ cell L}^{-1} \text{ day}^{-1}$. This result is consistent as the productivity inside photobioreactors is only controlled

by the reactor geometry (defining the illuminated specific surface) and by the light input, and independently of hydrodynamics (Pruvost et al., 2008). One exception appears when the microalgae are sensitive to light/dark cycle effects: a dynamic coupling occurs then between biological response and fluctuating light regimes encountered by flowing cells, thus implying an alteration of the photosynthetic conversion and a modification of the photobioreactor efficiency (Janssen et al., 2000; Richmond, 2004). Here, this phenomenon does not a priori exist due to the small incident flux applied.

For identical conditions ($q_0 = 250 \mu\text{mol m}^{-2} \text{s}^{-1}$, $D = 0.36 \text{ day}^{-1}$), the theoretical productivity was close to $3.0 \times 10^{10} \text{ cell L}^{-1} \text{ day}^{-1}$ (Fig. 6b), and thus is rather in agreement with the experimental one. The difference can be explained by: (i) experimental uncertainties (cell counting, fluctuating dilution rate), (ii) the assumptions associated with light transfer modeling (collimated incident flux, optical properties and cellular mass of *Isochrysis affinis galbana*).

It is now interesting to compare these results with larval needs in hatcheries which, as aforementioned, are averaged to $1.2 \times 10^{12} \text{ cell day}^{-1}$. By considering $P_x = 1.64 \times 10^{10} \text{ cell L}^{-1} \text{ day}^{-1}$, the daily microalgal production is, in this single-module photobioreactor, $10^{11} \text{ cell day}^{-1}$ and, by extrapolating to a 120-L multimodule one, $2 \times 10^{12} \text{ cell day}^{-1}$. Such latter volume would enable the averaged larval requirements to be covered. Note that the multimodule photobioreactor should be designed so as to adjust its microalgal production to the hatchery size, by modifying either the number of modules (i.e., the culture volume) or, the light flux (see Fig. 6b). For the highest productions, another alternative is to use several identical multimodule photobioreactors in parallel.

A strict comparison in terms of volumetric productivity with other commercialized systems remains difficult to set up as the complete set of parameters (i.e., microalga type, incident light flux, dilution rate, system geometry) is not most often available. Nevertheless, the main two competing photobioreactors encountered in aquaculture can be mentioned:

- the CAPS systems from the SeaSalter-Shellfish[®] Company (Kent, UK); they are bags or sleeve polyethylene reactors, suspended from a framework or supported within a mesh frame, indoors or outdoors, in which the culture is mixed by bubbling air (<http://www.seacaps.com/specs.htm>);
- the Biofence[®] photobioreactor (Cell Pharm[®] company) based on tubular units consisting of a vertical array of horizontal tubes connected to manifolds in a fence-like configuration. Each block is composed of 16 tubes with a 5 m length and a 0.03 m diameter (http://www.variconacqua.com/new_page_2.htm).

Finally, Figure 12 presents some photographs illustrating fouling deposition at internal walls after 40 days of con-

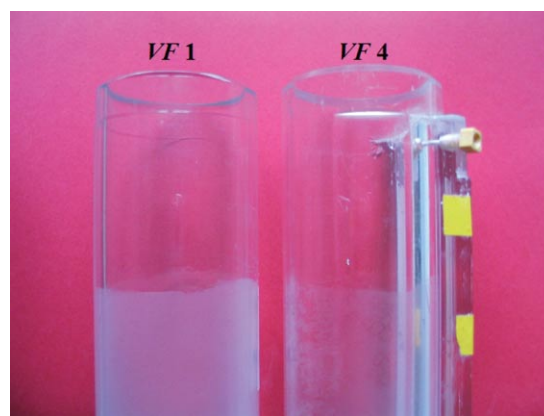


Figure 12. Photograph illustrating the biofouling deposited at walls after 40 days of *Isochrysis affinis galbana* continuous cultures, in the cases where an axial flow (VF1) and a swirling flow (VF4) are generated. [Color figure can be seen in the online version of this article, available at www.interscience.wiley.com.]

tinuous cultures, submitted to an axial (VF1) or a swirling flow (VF4). It clearly demonstrates that the microalgal deposition is significantly lower when a swirling motion is generated. Even if no fine analysis has been performed here to understand how local hydrodynamics affects biofouling, it is reasonable to suppose that this result is closely related to hydrodynamic characteristics inherent to swirling flows, namely: a high turbulence intensity, great tangential components of velocity close to walls (Fig. 8) and high levels of wall friction (Gupta et al., 1984; Legentilhomme and Legrand, 1991; Pruvost et al., 2000). This ability of swirling flows to limit the biofilm formation is particularly interesting for long-term continuous cultures because it suggests that the reactor walls could be maintained almost transparent. This will be helpful to prevent the irradiance received by microalgae from decreasing as long as the biofilm is depositing at walls. This phenomenon should not be neglected as it can induce a long-term reduction in productivity.

To conclude, the continuous cultures run in the single-module photobioreactor have shown that (i) the volumetric productivity is equal to $1.64 \times 10^{10} \pm 3 \times 10^8 \text{ cell L}^{-1} \text{ day}^{-1}$ and remains constant whatever the hydrodynamic conditions ($q_0 = 250 \mu\text{mol m}^{-2} \text{s}^{-1}$, $D = 0.36 \text{ day}^{-1}$), (ii) the microalgal production required in hatcheries can be satisfied, (iii) the microalgal deposition at walls is reduced when a swirling flow is generated instead of an axial one. In the specific context of hatcheries, these three points offer undeniable advantages as the continuous microalgal cultures have to be run during several months with a productivity that should remain constant for optimizing larvae feeding.

Conclusion

The present work has reported investigations carried out to optimize both design elements and dimensions of a new

photobioreactor for continuous production in mollusk hatcheries. The design has preliminarily been turned into an external-loop airlift configuration based on a succession of elementary modules, each one being composed of two transparent vertical interconnected columns. The liquid circulation is ensured pneumatically with respect to a swirling motion (tangential inlets). A single module of the whole photobioreactor was built up. Firstly, the two-flux radiative transfer model was adapted to account for refraction effects (front surface curvature) and for the optical properties of *Isochrysis affinis galbana*. The growth curve of this microalga was determined by using a planar torus photobioreactor and modeled with respect to a Monod law. By coupling the previous light and growth models, the volumetric productivities were predicted as a function of incident light flux, dilution rate and column radius. These results have revealed that a column radius of 0.03 m represents a good compromise between productivity and building cost price; therefore, this radius will be retained for scaling the multimodule photobioreactor. In a second step, the hydrodynamics of the liquid phase was modeled in terms of global flow behavior (mean circulation velocity, Péclet number) and of swirling motion decay. The generation of a swirling flow motion was logically proven positive for enhancing mixing. Whatever the operating conditions, the swirling motion, characterized by high tangential components of velocity, was conserved but significantly attenuated along the column. Thus, it is reasonable not to exceed a column height of 1 m for the multimodule system. In a third time, the aeration performances were determined by overall volumetric mass transfer coefficient measurements and demonstrated that the single-module photobioreactor had the physical capacity to remove the oxygen produced photosynthetically. Finally,

Isochrysis affinis galbana continuous cultures were run for geometrical configurations generating either an axial or a swirling motion (the other conditions remaining similar: $q_0 = 250 \mu\text{mol m}^{-2} \text{s}^{-1}$, $D = 0.36 \text{ day}^{-1}$). In both cases, the same productivity was reached: $1.64 \times 10^{10} \pm 3 \times 10^8 \text{ cell L}^{-1} \text{ day}^{-1}$. When accounting for experimental sensitivity and light modeling assumptions, this value was found to agree with the predicted data. Although no influence of hydrodynamics existed on productivity, some differences appeared in terms of biofouling. Indeed, the film deposited at walls was significantly thinner when a swirling motion was generated. To maintain high biological performances for long-term continuous cultures, such result is of great importance.

Coupled with technico-economical considerations, these investigations led us to design and build up a 120-L prototype made of 18 elementary modules (0.06 m in diameter, 1 m in length) connected by flanges equipped with VF4 prisms. As illustrated in Figure 13, the fluorescent lamps are inserted between columns and uniformly spaced. The column assembly was optimized to restrict floor-space ($1 \text{ m} \times 1.1 \text{ m} \times 1.65 \text{ m}$). Air injections were regularly dispatched in the prototype and performed by using capillaries placed tangentially to walls at the column base. The prototype can pivot according to a horizontal axis, thereby making cleaning and sterilization steps easier and less manpower intensive. *Isochrysis affinis galbana* continuous cultures were successfully run in this prototype (results not exposed here) and led to a microalgal production of stable quality and quantity under controlled conditions. In addition, this system offers other advantages for optimizing the mollusk larvae feeding: (i) it is expandable in elementary modules (i.e., adjustable to the microalgal production required), (ii) it is based on a pneumatic agitation (lower



Figure 13. Photographs of the 120-L multimodule photobioreactor (top and front views). [Color figure can be seen in the online version of this article, available at www.interscience.wiley.com.]

power input and more respectful for cell integrity), (iii) the fouling at walls is minimized. Currently, this prototype has been implemented in a French mollusk hatchery (Vendée Naissain[®]) and will be commercialized by the company Jouin Solutions Plastiques[®].

Nomenclature

b	backward scattering coefficient
C	tracer concentration inside the reactor (mol m^{-3})
C_L	dissolved oxygen concentration inside the liquid phase (mol m^{-3})
C_L^*	dissolved oxygen concentration at saturation inside the liquid phase (mol m^{-3})
C_P	dissolved oxygen concentration inside the probe (mol m^{-3})
C_∞	final tracer concentration inside the reactor (mol m^{-3})
D	dilution rate (s^{-1})
D_{ax}	axial dispersion coefficient ($\text{m}^2 \text{s}^{-1}$)
E_a	mass absorption coefficient ($\text{m}^2 \text{kg}^{-1}$)
E_s	mass scattering coefficient ($\text{m}^2 \text{kg}^{-1}$)
G	spherical irradiance ($\mu\text{mol m}^{-2} \text{s}^{-1}$)
G_C	compensation irradiance ($\mu\text{mol m}^{-2} \text{s}^{-1}$)
K_G	limitation constant ($\mu\text{mol m}^{-2} \text{s}^{-1}$)
k_{La}	overall volumetric mass transfer coefficient (s^{-1})
L	light path length (m)
L_t	mean reactor length ($L_t = 2.32$ m) (m)
Pe_L	Péclet number based on the mean reactor length ($Pe_L = U_C L_t / D_{ax}$)
P_X	volumetric microalgal productivity ($\text{cell m}^{-3} \text{s}^{-1}$)
q_O	averaged incident radiant light flux on the reactor surface, commonly named in photobioreactor studies Photon Flux Density (PFD) ($\mu\text{mol m}^{-2} \text{s}^{-1}$)
r	radial coordinate inside the column (m)
R	radius of the single-module photobioreactor column (m)
Sn	swirl number
t	time (s)
t_C	mean circulation time (s)
t_m	mixing time defined using a homogeneity degree equal to 95% (s)
t_p	time constant of the oxygen probe (s)
U	axial component of time-averaged velocity (m s^{-1})
U_C	mean circulation velocity (m s^{-1})
U_G	superficial gas velocity defined with respect to the column section ($\text{m}^2 \text{s}^{-1}$)
V_L	total liquid volume inside the single-module photobioreactor (m^3)
VF	Velocity Factor
W	tangential component of time-averaged velocity (m s^{-1})
x	axial coordinate inside the downcomer column, the origin being at the top (m)
X	cellular concentration (cell m^{-3})
z	position along the culture depth (m)
z^*	geometrical distance between tracer injection and detection points

Greek Letters

α	linear scattering modulus
δ	two-flux extinction coefficient (m^{-1})
ε_G	mean gas hold-up inside the pilot
μ	specific growth rate (s^{-1})

μ_m	maintenance term linked to respiration (s^{-1})
μ_{max}	maximal specific growth rate (s^{-1})
θ	ratio between time and mean circulation time
θ_C	angular position inside the column (radian)

The development of this work was made possible by the technical and financial support (CIFRE fellowship) of the plastic company Jouin Solutions Plastiques[®] (www.jouin.com); the authors are especially grateful for helpful discussions and suggestions provided by Jean-Claude Jouin. The authors would like to acknowledge also the French Region Pays-de-la-Loire for partly supporting this work through SMIDAP research program. Thanks to Loic Le Déan (Ifremer Nantes) for his technical help.

References

- Aoubed H, Legentilhomme P, Nouar C, Legrand J. 1994. Experimental comparison of electrochemical and dot-paint methods for the study of swirling flow. *J Appl Electrochem* 24:619–625.
- Benkhelifa H, Legrand J, Legentilhomme P, Montillet A. 2000. Study of the hydrodynamic behavior of the batch and continuous torus reactor in laminar and turbulent flow regimes by means of tracer methods. *Chem Eng Sci* 55:1871–1882.
- Borowitzka MA. 1997. Microalgae for aquaculture: Opportunities and constraints. *J Appl Phycol* 9:393–401.
- Carvalho AP, Meireles LA, Malcata FX. 2006. Microalgal reactors: A review of enclosed system designs and performances. *Biotechnol Prog* 22: 1490–1506.
- Chisti YM. 1989. *Airlift bioreactors*. London, England: Elsevier Applied Science.
- Cornet J-F, Dussa C-G, Gros J-B. 1995. A simplified monodimensional approach for modeling coupling between radiant light transfer and growth kinetics in photobioreactors. *Chem Eng Sci* 50(9):1489–1500.
- Coulteau P, Sorgeloos P. 1992. The use of algal substitutes and the requirement for live algae in hatchery and nursery rearing of bivalve mollusks: An international survey. *J Shellfish Res* 11:467–476.
- Falkowski PG, Dubinsky Z, Wyman K. 1985. Growth-irradiance relationships in phytoplankton. *Limnol Oceanogr* 30(2):311–321.
- Green JC, Leadbeater BSC. 1994. *The Haptophyte algae*. Oxford, England, The Systematics Association special volume ISBN 0-198-57772-9 446.
- Gupta A, Lilley DG, Syred N. 1984. *Swirl flow*. Energy and engineering sciences series. Cambridge: Abacus Press.
- Hébrard G, Bastoul D, Roustan M. 1996. Influence of the gas sparger on the hydrodynamic behavior of bubble columns. *Trans IChem E* 74(A):406–414.
- Ingham J, Dunn IJ, Heinzle E, Prenosil JE. 1994. *Chemical engineering dynamics, modeling with PC simulation*. New York, USA: VCH publishers, Inc. ISBN 3-527-28577-6.
- Janssen M, Janssen M, de Winter M, Tramper J, Mur LR, Wijffels RH. 2000. Efficiency of light utilization of *Chlamydomonas reinhardtii* under medium-duration light/dark cycles. *J Biotechnol* 78:123–137.
- Legentilhomme P, Legrand J. 1991. The effects of inlet conditions on mass transfer in annular swirling decaying flow. *Int J Heat Mass Transfer* 34:1281–1291.
- Loubière K, Hébrard G, Guiraud P. 2003. Dynamics of bubble growth and detachment from rigid and flexible orifices. *Can J Chem Eng* 81(3–4): 499–507.
- Molina Grima E, García Camacho F, Sanchez Perez JA, Acien Fernández FG, Fernandez Sevilla JM. 1997. Growth yield determination in a chemostat culture of the marine microalga *Isochrysis galbana*. *J Appl Ecol* 8:529–534.
- Muller-Feuga A, Le Guedes R, Pruvost J. 2003a. Benefits and limitations of modeling for optimization of *Porphyridium cruentum* cultures in an annular photobioreactor. *J Biotech* 102(2):153–163.

- Muller-Feuga A, Pruvost J, Le Guedes R, Le Dean L, Legentilhomme P, Legrand J. 2003b. Swirling flow implementation in a photobioreactor for batch and continuous cultures of *Porphyridium cruentum*. *Biotech Bioeng* 84(5):544–551.
- Pottier L, Pruvost J, Deremetz J, Cornet J-F, Legrand J, Dussap CG. 2005. A fully predictive model for one-dimensional light attenuation by *Chlamydomonas reinhardtii* in a torus photobioreactor. *Biotech Bioeng* 91(5):569–582.
- Pruvost J, Legrand J, Legentilhomme P. 2000. Particle image velocimetry investigation of the flow-field of a 3D turbulent annular swirling decaying flow induced by means of a tangential inlet. *Exp Fluids* 29: 291–301.
- Pruvost J, Legrand J, Legentilhomme P, Muller-Feuga A. 2002. Simulation of microalgae growth in limiting light conditions. *AIChE J* 48(5):110–1120.
- Pruvost J, Pottier L, Legrand J. 2006. Numerical investigation of hydrodynamic and mixing conditions in a torus photobioreactor. *Chem Eng Sci* 61(14):4476–4489.
- Pruvost J, Cornet J-F, Legrand J. 2008. Hydrodynamics influence on light conversion in photobioreactors: An energetically consistent analysis. *Chem Eng Sci* 63:3679–3694.
- Richmond A. 2004. *Handbook of microalgal mass culture: Biotechnology and applied phycology*. Oxford: Wiley-Blackwell.
- Rico-Villa B, Le Coz JR, Mingant C, Robert R. 2006. Influence of phytoplankton diet mixtures on microalgae consumption, larval development and settlement of the Pacific oyster *Crassostrea gigas* (Thunberg). *Aquaculture* 256(1–4):377–388.
- Roustan M. 2003. *Transferts gaz-liquide dans les procédés de traitement des eaux et des effluents gazeux*. Paris: Editions Dec & Doc.
- Spolaore P, Joannis-Cassan C, Duran E, Isambert A. 2006. Review: Commercial applications of microalgae. *J Biosci Bioeng* 101(2):87–96.
- Sukenik A, Wahnon R. 1991. Biochemical quality of marine unicellular algae with special emphasis on lipid composition. I. *Isochrysis galbana*. *Aquaculture* 97(1):61–72.
- Tzovenis I, De Pauw N, Sorgeloos P. 2003. Optimization of T-iso biomass production rich in essential fatty acids I. Effect of different light regimes on growth and biomass production. *Aquaculture* 216(1–4):203–222.
- Vandu CO, Koop K, Krishna R. 2004. Volumetric mass transfer coefficient in a slurry bubble column operating in the heterogeneous flow regime. *Chem Eng Sci* 59:5417–5423.
- Wu WT, Wu JY, Jong JZ. 1992. Mass transfer in an airlift reactor with a net draft tube. *Biotechnol Prog* 8(5):465–468.